Numerical Investigation of the Linear Stability of a Free Convection Boundary Layer Flow Using a Thermal Disturbance With a Slowly Increasing Frequency

Manosh C. Paul
Department of Mechanical Engineering,
University of Glasgow,
Glasgow G12 8QQ, UK
e-mail: m.paul@mech.gla.ac.uk

D. Andrew S. Rees
Department of Mechanical Engineering,
University of Bath,
Bath BA2 7AY, UK

Numerical simulations are performed to investigate the linear stability of a two-dimensional incompressible free convection flow induced by a vertical semi-infinite heated flat plate. A small-amplitude local temperature disturbance with a slowly increasing frequency is introduced on the surface near to the leading edge in order to generate disturbance waves within the boundary layer. The aim is to compare the response of the thermal boundary layer with that obtained by selecting discrete disturbance frequencies. In the present study, air is considered to be the working fluid for which the value of the Prandtl number is taken to be $Pr=0.7$. The computational results show that the disturbance decays initially until it reaches a critical distance, which depends on the current frequency of the disturbance. Thereafter the disturbance grows, but the growth rate also depends on the effective frequency of the disturbance. Comparisons with previous work using constant disturbance frequencies are given, and it is shown that the sine-sweep technique is an effective method for analyzing the instability of convectively unstable boundary layers. [DOI: 10.1115/1.2976554]

Keywords: numerical simulation, free convection, linear stability, receptivity, sine sweep

1 Introduction

In the free convection boundary layer flow over a vertical surface, the primary mode of instability takes the form of two-dimensional waves, which travel in the streamwise direction. This is well known to be a hydrodynamic instability [1,2] even though the basic state is generated by buoyancy forces and the flow is advectively unstable as opposed to being absolutely unstable.

Goldstein [3] in the study of evolution of Tollmien–Schlichting waves recognized that near the leading edge, but not so near that the fully elliptic equations have to be considered, the boundary layer is fairly thin and grows rapidly in the downstream direction compared with the situation further downstream. In this region the parallel flow assumption is inaccurate. On the other hand, at greater distances from the leading edge, the parallel flow approximation holds and the linear stability properties of the flow can be fairly accurately predicted by the thermal equivalent of the Orr–Sommerfeld equation. In the free convection boundary layer flow, Paul [4] and Paul et al. [5] also showed that the linear stability results based on the parallel flow approximation (Paul et al. [6]) agree well with the results obtained from full unsteady 2D simulations at large downstream distances, but that there is poor agreement near the leading edge region. It was concluded that it is necessary to solve the full unsteady 2D equations in order to obtain accurate predictions of the stability characteristics near the base of the neutral curve rather than to use the parallel flow approximation.

In Refs. [4,5], the stability of the free convection thermal boundary layer flow from a vertical flat plate was studied by introducing the following thermal disturbances: (i) an isolated internal disturbance at one point in time and (ii) a time-periodic local variation in the surface temperature near the leading edge of the flat plate. When the point thermal disturbance was introduced, it was found that, as time progresses, the disturbance diffuses and travels downstream, leaving behind an undisturbed flow. The spatial wavelength of the traveling cells also increases, which is consistent with the fact that the base flow accelerates in the streamwise direction. In addition, the variation of the surface rate of heat transfer with time showed a distinctive time scale or frequency associated with the evolving disturbance. The latter disturbance may be regarded as being of similar type to the suction strip approach of Fasel and Konzelmann [7], the oscillating heat source of Brooker et al. [8], and the vibrating ribbon experiments of Dietz [9]. Such thermal disturbances produce instability waves of Tollmien–Schlichting type into the otherwise steady flow, and then the magnitude of the waves either grows or decays roughly in accordance with linear stability theory analysis such as was performed by Paul et al. [6] using the parallel flow approximation.

In addition, for the time-periodic thermal oscillation [4,5], sinusoidal thermal disturbances of fixed frequency were introduced near the leading edge of a flat plate to generate wavelike instabilities in order to study the stability and thermal receptivity of the boundary layer flow. A large range of different frequencies were introduced in order to trace out a neutral stability curve based on the full elliptic system of equations. The main purpose of the present paper is to revisit this stability problem by using thermal disturbances with a gradually increasing frequency. In other engineering contexts this procedure is referred as a sine-sweep. If the sine-sweep method were shown to be able to reproduce the sta-

---

Contributed by the Heat Transfer Division of ASME for publication in the Journal of Heat Transfer. Manuscript received September 19, 2007; final manuscript received May 22, 2008; published online September 18, 2008. Review conducted by Cholik Chan.

bility characteristics of the boundary layer accurately, then it could be used to replace a very large number of simulations with one albeit lengthy simulation. In our application of the sine-sweep idea a slow variation of the effective frequency is used, and the stability properties of the boundary layer are compared with those obtained in Refs. [5,6] in order to determine the applicability of the sine-sweep idea.

The sine-sweep idea may also be applied to experimental setups in order to determine the stability characteristics of the boundary layer. This would also yield important information such as neutral curves and local growth rates relatively quickly.

2 Governing Equations and Boundary Conditions

We consider the two-dimensional incompressible free convection boundary layer flow over a vertical infinite span heated plate where x is the streamwise coordinate and y is the wall-normal coordinate. A detailed schematic of the flow configuration may be found in Ref. [5]. The equations of motion of the free convective boundary layer flow are taken to be the incompressible Navier–Stokes and energy transport equations. For unsteady two-dimensional flow this system, subject to the Oberbeck–Boussinesq approximation, may be written in nondimensional stream function (ψ), vorticity (ω), and temperature (θ) form [5] as

$$\frac{\partial^2\psi}{\partial x^2}+\frac{\partial^2\psi}{\partial y^2}=\omega \tag{1}$$

$$\frac{\partial\omega}{\partial t}=\frac{\partial^2\omega}{\partial x^2}+\frac{\partial^2\omega}{\partial y^2}+\frac{\partial\psi}{\partial x}\frac{\partial\omega}{\partial y}-\frac{\partial\psi}{\partial y}\frac{\partial\omega}{\partial x}+\frac{\partial\theta}{\partial y} \tag{2}$$

$$\frac{\partial\theta}{\partial t}=\frac{1}{\Pr}\left(\frac{\partial^2\theta}{\partial x^2}+\frac{\partial^2\theta}{\partial y^2}\right)+\frac{\partial\psi}{\partial x}\frac{\partial\theta}{\partial y}-\frac{\partial\psi}{\partial y}\frac{\partial\theta}{\partial x} \tag{3}$$

where the stream function (ψ) is defined such that $u=\psi_y$ and $v=-\psi_x$. Here u and v are the nondimensional velocity components along the x and y coordinate directions, respectively. The constant Pr is the fluid Prandtl number. The detailed nondimensionalizations of the full governing equations are given in Refs. [4,5]. We note that the length scale used is a natural one based on the properties of the fluid and the temperature drop. Therefore no Grashof number appears in the equations, as $\mathrm{Gr}=1$ defines this natural length scale. The boundary layer approximation is now equivalent to $x\gg 1$.

On applying the Schwartz–Christoffel transformation $3(\xi+i\eta)=[4(x+iy)]^{3/4}$ into Eqs. (1)–(3) and introducing a small disturbance into the steady flow for which we set

$$\psi(\xi,\eta,t)=\bar{\psi}(\xi,\eta)+\delta\hat{\psi}(\xi,\eta,t) \tag{4}$$

$$\omega(\xi,\eta,t)=\bar{\omega}(\xi,\eta)+\delta\hat{\omega}(\xi,\eta,t) \tag{5}$$

$$\theta(\xi,\eta,t)=\bar{\theta}(\xi,\eta)+\delta\hat{\theta}(\xi,\eta,t) \tag{6}$$

the following linearized perturbation equations are obtained:

$$\frac{\partial^2\hat{\psi}}{\partial\xi^2}+\frac{\partial^2\hat{\psi}}{\partial\eta^2}=A\hat{\omega} \tag{7}$$

$$\begin{aligned}A\frac{\partial\hat{\omega}}{\partial t}&=\frac{\partial^2\hat{\omega}}{\partial\xi^2}+\frac{\partial^2\hat{\omega}}{\partial\eta^2}+A^{1/2}\left(\frac{\partial\hat{\theta}}{\partial\xi}\sin\frac{1}{4}\phi+\frac{\partial\hat{\theta}}{\partial\eta}\cos\frac{1}{4}\phi\right)\\&\quad+\left(\frac{\partial\bar{\omega}}{\partial\eta}\frac{\partial\hat{\psi}}{\partial\xi}-\frac{\partial\bar{\omega}}{\partial\xi}\frac{\partial\hat{\psi}}{\partial\eta}\right)+\left(\frac{\partial\bar{\psi}}{\partial\xi}\frac{\partial\hat{\omega}}{\partial\eta}-\frac{\partial\bar{\psi}}{\partial\eta}\frac{\partial\hat{\omega}}{\partial\xi}\right)\end{aligned} \tag{8}$$

$$A\frac{\partial\hat{\theta}}{\partial t}=\frac{1}{\Pr}\left(\frac{\partial^2\hat{\theta}}{\partial\xi^2}+\frac{\partial^2\hat{\theta}}{\partial\eta^2}\right)+\left(\frac{\partial\bar{\psi}}{\partial\xi}\frac{\partial\hat{\theta}}{\partial\eta}-\frac{\partial\bar{\psi}}{\partial\eta}\frac{\partial\hat{\theta}}{\partial\xi}\right)+\left(\frac{\partial\bar{\theta}}{\partial\eta}\frac{\partial\hat{\psi}}{\partial\xi}-\frac{\partial\bar{\theta}}{\partial\xi}\frac{\partial\hat{\psi}}{\partial\eta}\right) \tag{9}$$

where δ in Eqs. (4)–(6) represents a small quantity, and therefore powers of δ have been neglected when deriving Eqs. (7)–(9). Furthermore, the overbar indicates the steady state base flow quantities while the hat (circumflex) denotes the perturbation variables. The quantity ϕ, which appears in Eq. (8), is the polar angle from the heated surface, while the function A is defined according to $A^3=\left(\frac{3}{4}\right)^2(\xi^2+\eta^2)^2$.

The corresponding boundary conditions that are needed to solve Eqs. (7)–(9) are

$$\hat{\psi}=\hat{\psi}_\eta=0,\quad \hat{\theta}=0\quad \text{on}\quad \eta=\eta_{\min}=0 \tag{10}$$

$$\hat{\psi}=\hat{\psi}_\xi=0,\quad \hat{\theta}_\xi=0\quad \text{on}\quad \xi=\xi_{\min} \tag{11}$$

$$\hat{\psi}_\eta=0,\quad \hat{\omega}=0,\quad \hat{\theta}=0\quad \text{as}\quad \eta=\eta_{\max} \tag{12}$$

while at the outflow ($\xi_{\max}$) we apply a buffer domain function in order to dampen down disturbances and to prevent unphysical reflections. Further details of the use of a buffer function are given in Sec. 3. It should be noted here that the leading edge of the heated surface was taken to be at $\xi_{\min}=20$, which corresponds to $x\simeq 37$ in Cartesian coordinates. The origin of the coordinate system is outside of the computational domain and therefore we define the new variable $x^*=x-37$, which is the distance to the leading edge. The parallel flow investigations (PFIs) [6] were carried out for the same x^*.

After solving for the basic state, $(\bar{\psi},\bar{\omega},\bar{\theta})$, using the procedure outlined in Sec. 3, a thermal disturbance is introduced by changing the surface temperature near the leading edge. Therefore we solve the linearized disturbance equations (7)–(9) subject to the no-slip condition on the surface and the thermal boundary condition

$$\hat{\theta}=e^{-a(\xi-\xi_0)^2}\sin(ct^2)\quad \text{at}\quad \eta=0 \tag{13}$$

where $\lambda=2ct$ is defined as the temporal frequency, which is a slowly varying function of time t. In Eq. (13) $\xi_0=20$ is the center of the region where the thermal disturbance is introduced. This region is located well upstream of where the boundary layer becomes unstable. In addition, $a=0.1$ was chosen such that the thermal disturbance region was well resolved on the computational grid but is still located fully upstream of the neutral point.

3 Numerical Method

Finite difference techniques are used to solve the system of nonlinear equations (1)–(3) and the system of linear equations (7)–(9). The overall accuracy of the numerical scheme is second order in both time and space.

The time-dependent equations are discretized using central differences and the DuFort–Frankel method for the time-derivative and diffusion terms. The Jacobian terms are approximated using the Arakawa [10] formulation, which was designed to be particularly suitable for unsteady flows. Derivative boundary conditions are approximated using a standard ghost point approach, which has a smaller discretization error than a one-sided first-order approximation.

The Poisson equation (7) was solved using a multigrid correction scheme algorithm to accelerate iterative convergence. It incorporates a V-cycle algorithm involving the line Gauss–Seidel relaxation procedure. The method is based on the pointwise method described in Ref. [11] but adopts two line relaxations per coordinate direction on each multigrid level.

The buffer domain technique of the outflow boundary follows the methodology introduced by Kloker et al. [12]. The naive imposition of boundary conditions involving either the first or second derivatives of the dependent variables results in the progressive upstream propagation of spatially pointwise oscillations, which eventually degrade the evolving solution. Kloker et al. [12] discussed at length six different strategies for dealing with outflow conditions and concluded that, for the Blasius boundary layer at least, a very satisfactory method is to use an absorbing buffer region. Such a region is used to damp out disturbances to the basic flow and is sometimes called a relaminarization region. The method has also been used very satisfactorily in other flows; see Refs. [13,14], for example. For the present problem the concept of a buffer region translates into setting

$$\chi_{\text{dist}}^{\text{new}} = F(\xi) \times \chi_{\text{dist}}^{\text{old}} \tag{14}$$

at each time step. Here χ represents either the vorticity or temperature, χ^{old} is the computed value of χ obtained using the DuFort–Frankel method subject to the boundary condition $\partial\chi/\partial\xi=0$ at $\xi=\xi_{\max}$, and χ^{new} is the value of χ, which is used to compute χ at subsequent time steps. The buffer function $F(\xi)$ takes the value of 1 in most of the computational domain and is a fifth-order polynomial in ξ, which decreases from 1 at the start of the buffer region to 0 at outflow. At both the beginning ($\xi=\xi_{b1}$) and the end ($\xi=\xi_{b2}$) of the buffer region the function has zero first and second derivatives. In more detail, the buffer function used was

$$F(\xi) = 1, \quad \xi < \xi_{b1}$$

$$F(\xi) = 1 - 10\gamma^3 + 15\gamma^4 - 6\gamma^5, \quad \xi_{b1} < \xi < \xi_{b2} \tag{15}$$

$$F(\xi) = 0, \quad \xi > \xi_{b2}$$

where $\gamma=(\xi-\xi_{b1})/(\xi_{b2}-\xi_{b1})$. For nonlinear problems, such as those involving the computation of the basic steady flow, the outflow formula (14) translates into the following form, which is suitable for solving for the true variables rather than for disturbances:

$$\chi^{\text{new}} = F(\xi) \times \chi^{\text{old}} + [1 - F(\xi)] \times \chi^{\text{basic}} \tag{16}$$

where χ^{basic} represents the basic boundary layer solutions of the corresponding variable (vorticity or temperature), which is obtained from the steady solutions of Eqs. (1)–(3).

In the simulation, $\xi_{\max}=620$ was chosen and the buffer region started from $\xi_{b1}=520$. A series of simulations was undertaken changing the position of the start of the buffer region, and the test results show that there was no effect on the solutions in the unbuffered region.

Initially, a total of 480 nodes were used in the ξ-direction with a uniform distribution of the mesh size of $d\xi=1.25$. In the y-direction we used 48 nodes and the domain extends to $\eta_{\max}=12$. In order to show grid independence test of our stability results, the above grid size was doubled, i.e., we used 960 nodes in the x-direction and 96 nodes in the y-direction. We have $\delta\xi=5\delta\eta$, which yields a cell aspect ratio of 5, and therefore a line relaxation method is essential. We were able to take five multigrid levels and each V-cycle was comprised of two relaxation sweeps in each coordinate direction for each grid. At each time step the vorticity and temperature fields are updated for the new time level, followed by the solution of the Poisson equation for the stream function, and finally the boundary vorticity is computed using the ghost point approach.

4 Results and Discussion

We have run simulations for three different values of the parameter c in Eq. (13): $c=10^{-4}$, $c=5\times10^{-5}$, and $c=2.5\times10^{-5}$, with a constant time step of $\delta t=0.01$. In Sec. 4.1, some computed results of the linear stability are presented for $c=5\times10^{-5}$, and a detailed comparison of the stability characteristics for the other values of c with the fixed frequency simulation of Ref. [5] is presented in Sec. 4.2.

In order to generate results up to the maximum effective frequency of $\lambda_{\max}=0.8$, for which the corresponding nondimensional time is $t_{\max}=8000$, we used a total of 4×10^5 time steps for $c=10^{-4}$. When the value of c is reduced to half of its original value, i.e., for $c=5\times10^{-5}$, the computational cost doubles and we required 8×10^5 time steps to achieve results up to $\lambda_{\max}=0.8$ or $t_{\max}=8000$. Similarly, we required 16×10^5 time steps for $c=2.5\times10^{-5}$.

We note that the value of δt is very small compared with the physical time scales over which variations of interest take place. In addition, the magnitude of c is chosen such that the frequency variation is slow enough that the transient results obtained for any frequency are very close to the results that were obtained when the flow was perturbed with a fixed frequency. This sine-sweep approach has often been used in other engineering contexts to determine, for example, the resonance characteristics of mechanical systems or the acoustic properties of cavities. It is, to our knowledge, the first time that it has been used to assess the stability characteristics of a thermal boundary layer.

4.1 Stability Results for $c=5\times10^{-5}$. Given that the effective temporal frequency in the sine-sweep disturbance (13) is a function of time (viz., $\lambda=2ct$), it is now possible to trace out the evolution of the thermal disturbance inside the boundary layer with respect to either time or frequency. In this regard we have plotted some isocontours of the temperature disturbance, $\hat{\theta}$, in Fig. 1 for $c=5\times10^{-5}$. The contour levels in each frame are set at $\pm10^{-n}\max_{x^*,y}|\hat{\theta}|$ for $n=1,2,\ldots,5$, and it must be noted that the wall-normal coordinate, y, has been stretched substantially in order to see the patterns clearly. The dashed contours correspond to negative values of $\hat{\theta}$ while the solid lines correspond to positive values of $\hat{\theta}$. The results in Fig. 1 are for various values of the disturbance frequency λ. The results shown in the lowest frame are for $\lambda=0.1$, which corresponds to the nondimensional time of $t=1000$, while the top frame is for $\lambda=0.75$ for which the corresponding time is $t=7500$.

The numerical values corresponding to the contour plots show that, for all values of λ, the thermal disturbances decay initially with x^* near the leading edge of the surface and then grow with x^*; this feature is easily seen in Fig. 1 for $\lambda>0.55$, and for $\lambda<0.55$ it is clearer in Fig. 3. The x^* locations where the disturbance begin to be amplified (i.e., the neutral location) depend on the forcing frequency λ. We find that, when $\lambda>0.5$, the initial decay of the thermal disturbances is substantial and that the neutral location moves downstream as λ increases. The neutral point location is indicated by the black triangles for $\lambda\geq0.5$.

In Fig. 1 we can also see that the length of the thermal cells increases with distance from the leading edge, thereby confirming that the basic flow accelerates, the streamwise velocity being roughly proportional to $x^{1/2}$. As time progresses, which corresponds to increasing the disturbance frequencies, the wavelength decreases. The effects of the buffer function used in the buffer region near the outflow at $x^*=3565$ are also noticeable, where the damping of the disturbances is clearly evident. Also it should be noted that the largest positive thermal wave located at the upstream of the start of the buffer domain takes a total of 136 spatial nodes when $\lambda=0.1$, while it is 26 when $\lambda=0.4$

The time evolution of the surface rate of heat transfer, $H(t)$, which was computed using the following relation:

$$H(x^*,t) = \left(\frac{\partial\hat{\theta}}{\partial\eta}\right)_{\eta=0} \tag{17}$$

has been plotted in Fig. 2 at (a) $x^*=16$ and (b) $x^*=207$ for the same value of c, i.e., $c=5\times10^{-5}$. Figure 2(a) shows that the mag-

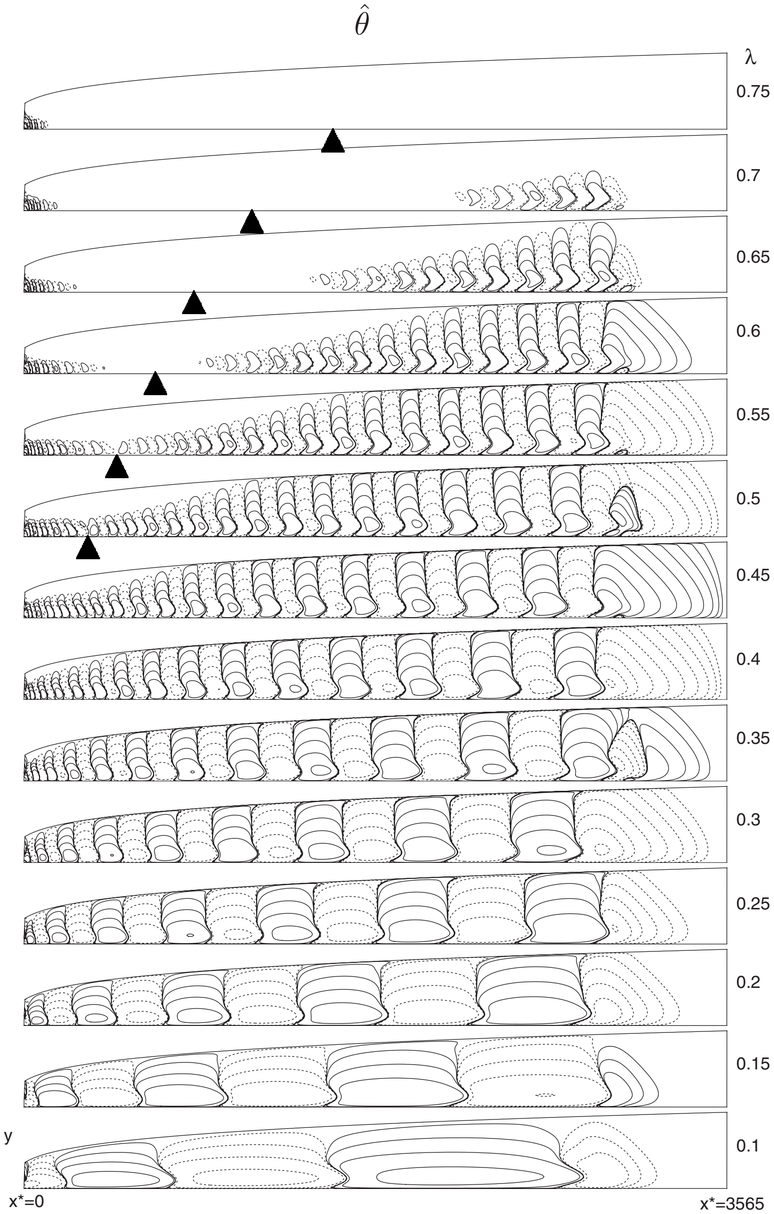

Fig. 1 Contours of $\hat{\theta}$ recorded at various values of the temporal frequency, λ, for $c=5\times10^{-5}$. Here ten contour levels are plotted based on the global extrema within each frame (see the text of the paper). The dashed contour lines represent negative values of $\hat{\theta}$ while the solid lines represent positive $\hat{\theta}$.

nitude of the disturbance decays for all time as this location is close to the leading edge of the vertical surface and well upstream of the neutral location, $x^*=147$, determined by Paul et al. [6]. On the other hand, Fig. 2(*b*) shows that the disturbance grows until t is just below 3000 and then decays, as this distance is well above downstream of the neutral location. The dashed lines in both frames indicate the envelope of the local maximum responses; and for the other x^* locations, these envelopes are plotted in Fig. 3 using a log scale.

In Fig. 3 the envelopes of the maximum response of the thermal disturbance in terms of the surface rate of heat transfer are displayed against time t for a selection of locations along the boundary layer. The results are calculated at various locations along the heated surface using the following relation:

$$Q(x^*,t) = \text{envelope}\left\{\log_{10}\left|\left(\frac{\partial\hat{\theta}}{\partial\eta}\right)_{\eta=0}\right|\right\} \qquad (18)$$

This equation defines a surface in (x^*,t)-space or equivalently in (x^*,λ)-space.

The variation of Q at $x^*=16$ (i.e., at $x=53$) shows that Q decays for all time, which is not surprising, and it is, indeed, expected, since this location is very close to the leading edge of the surface and it lies well below the critical/neutral distance ($x^*=147$) of the neutral curve obtained by Paul et al. [6]. The next four curves in Fig. 3 are at $x^*=34$ (i.e., at $x=71$), $x^*=52$ (i.e., at $x=89$), $x^*=72$ (i.e., at $x=109$), and $x^*=93$ (i.e., at $x=130$), respectively, and since these are also below the critical distance no growth of the

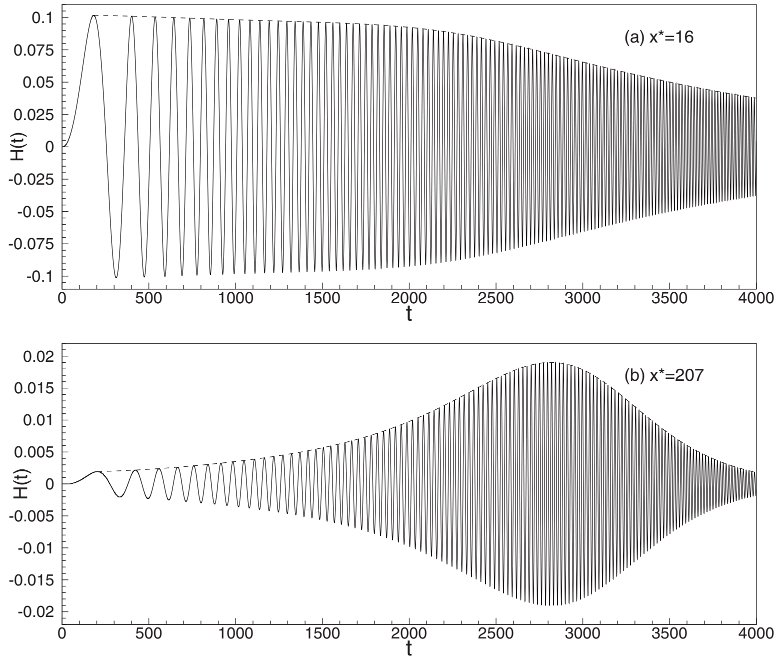

Fig. 2 Time variation of the surface rate of heat transfer recorded at (*a*) $x^*=16$ and (*b*) $x^*=207$ where $c=5\times10^{-5}$

thermal disturbance is observed. Thus the results obtained from the elliptic calculations approximately coincide with the results from the parallel flow analysis of Paul et al. [6]. At larger values of x^*, the corresponding curves show that there is a frequency interval within which the disturbances grow. The frequencies of maximum disturbance amplification for any given distance, x^*, which are plotted as a dotted line in the figure, show clearly that the disturbances also grow in space for any given frequency—this aspect will be looked at more closely in Figs. 4–7 and summarized later.

The uppermost curve in Fig. 3 corresponds to $x^*=2813$ (i.e., $x=2850$), which is just upstream of the buffer region, and this is the location where the disturbances are expected to reach their largest values. In the buffer zone no growth of the disturbances is achieved as its purpose is to dampen down the disturbances and remove unphysical reflections near the outflow boundary.

While Fig. 3 shows the variation of the disturbance amplitude with time, t, for a set of values of x^*, Fig. 4 shows its variation with x^* at chosen times or, equivalently, at chosen effective frequencies, λ. From this figure we can see that the disturbance amplitude decays for all frequencies when x^* is sufficiently close to the leading edge. As mentioned before, this region is within the stable region of the neutral curve. The curve corresponding to $\lambda=0.1$ is almost horizontal after the initial decay, indicating that disturbances of this frequency are almost neutral, i.e., they neither grow nor decay. However, when λ takes larger values we see very evident regions of decay and growth. Neutral locations correspond to minima in these curves, which are denoted by circles.

The frequency for which the largest disturbance amplitude is obtained at a given downstream location depends on x^*; this is

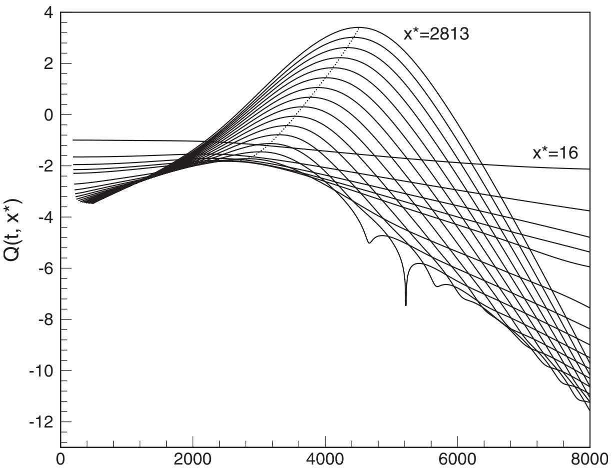

Fig. 3 Envelope of the maximum heat transfer response, *Q*, against time for various locations along the heated surface where $c=5\times10^{-5}$

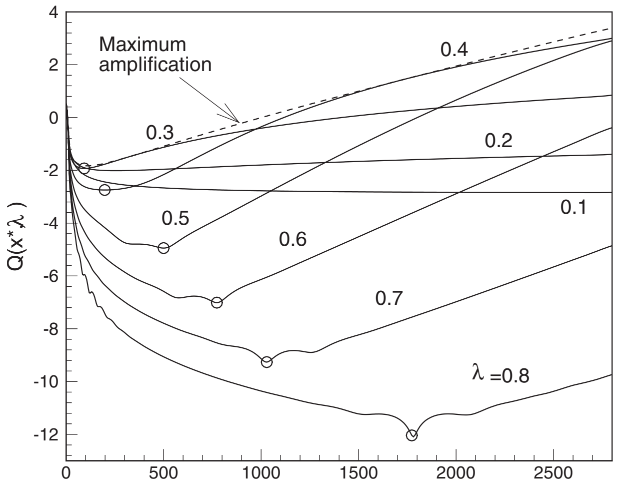

Fig. 4 Envelope of the maximum heat transfer response, *Q*, against distance for various disturbance frequencies, where $c=5\times10^{-5}$

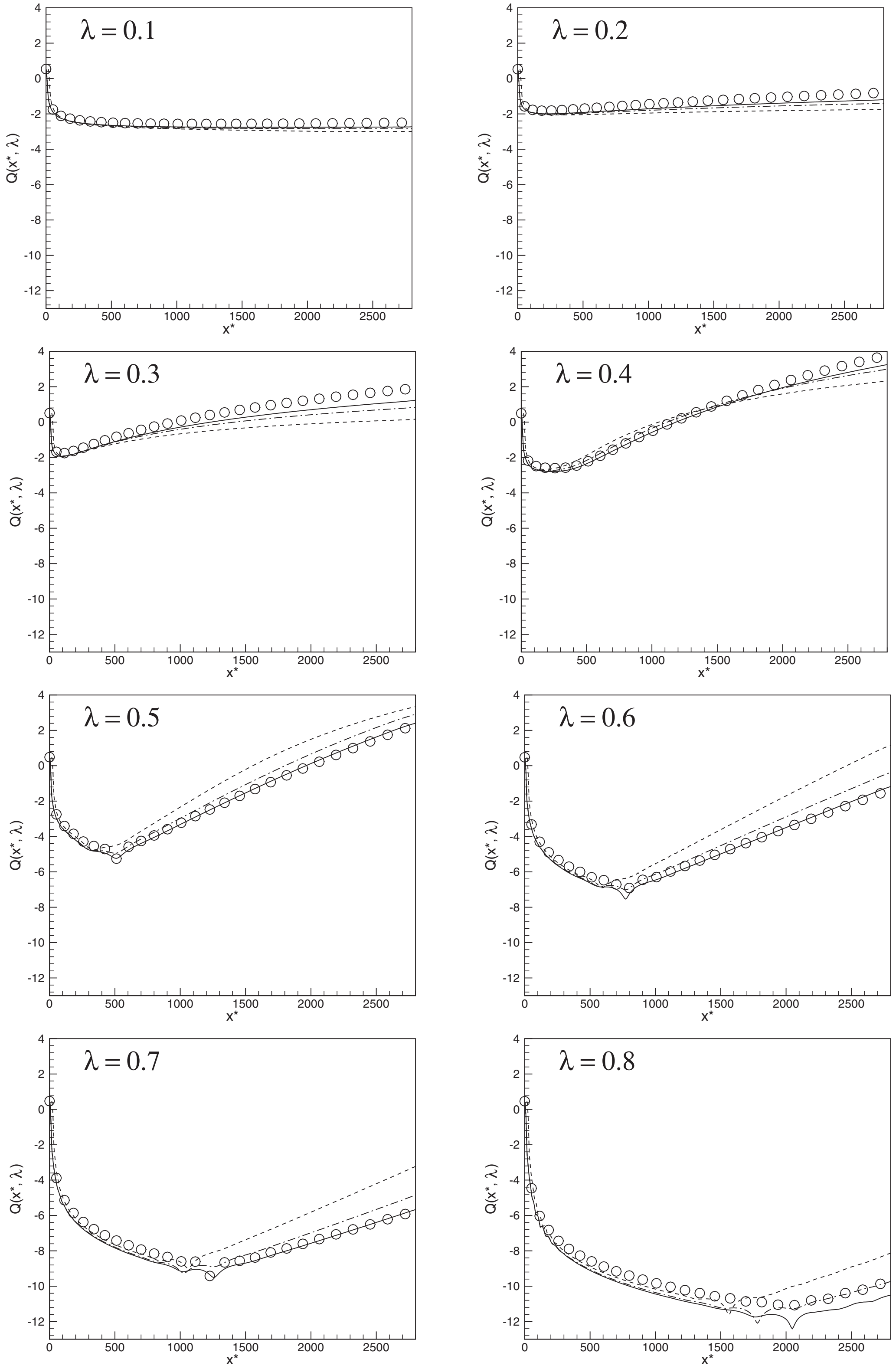

Fig. 5 Comparison of Q for the three different values of c and the discrete frequency [5]. The dashed lines are for $c=10^{-4}$, the dashed-dotted lines are for $c=5\times10^{-5}$, the solid lines are for $c=2.5\times10^{-5}$, and the circles are for the discrete frequency results.

illustrated clearly in Fig. 4 by the dashed line. For example, near to $x^{*}=500$, the frequency $\lambda=0.3$ gives the maximum amplitude, while near the buffer domain, values of λ that are closer to 0.4 yield the greatest response.

4.2 Results for the Different Values of c.

In this section we summarize the stability results that have been presented in Sec. 4.1 and we also give a detailed comparison of those obtained for the other values of the parameter c with the discrete frequency [5].

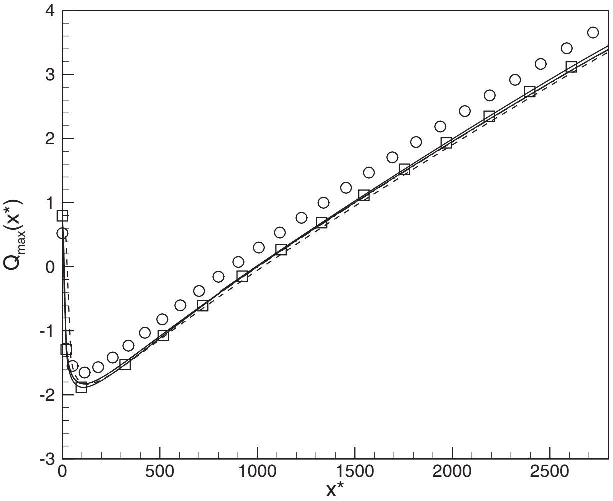

Fig. 6 The envelope of the curves presented in Figs. 4 and 5. For legends, see Fig. 5. The solid line with square symbols denotes the results for $c=2.5\times10^{-5}$ obtained by the finer grid, 960×96.

With this in mind, the envelope of the maximum surface heat transfer rate, $Q(x^*,\lambda)$, has been computed for the other two values of c, namely, $c=10^{-4}$ and $c=2.5\times10^{-5}$, and these are plotted in Fig. 5 along with the results for $c=5\times10^{-5}$ and the fixed frequency results.

The circles in each frame of Fig. 5 represent the results obtained by Paul et al. [5], which were obtained with constant frequency forcing. The sine-sweep simulation results are plotted as the dashed lines for $c=10^{-4}$, while the dashed-dotted lines are the results for $c=5\times10^{-5}$ and the solid lines are for $c=2.5\times10^{-5}$. This figure shows clearly that the qualitative agreement of the sine-sweep results with the fixed frequency results is very good. The results of $c=2.5\times10^{-5}$ have also an excellent quantitative agreement with the fixed frequency for $0.5<\lambda<0.7$, but when $\lambda=0.8$, it appears that the results of $c=5\times10^{-5}$ show better agreement with the fixed frequency results. In the first three frames, when $\lambda<0.4$, the $c=2.5\times10^{-5}$ results deviate slightly from the fixed frequency results in the downstream section of the boundary layer.

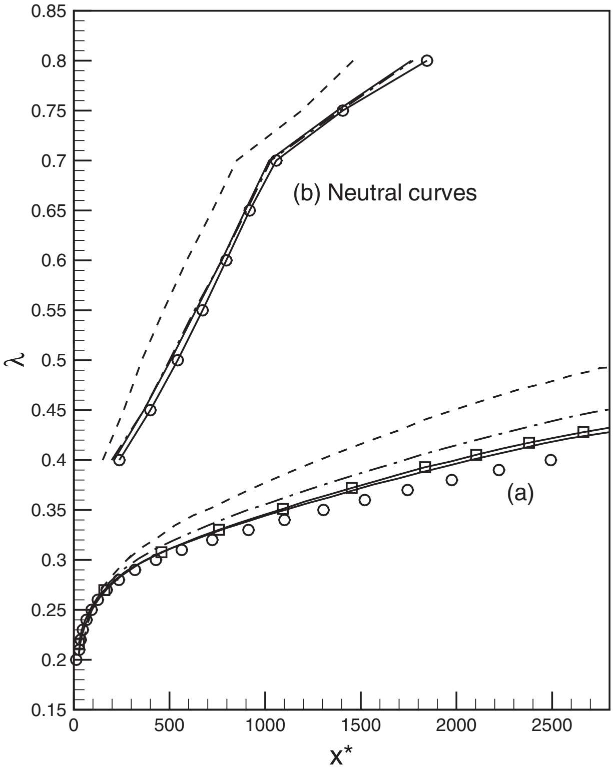

Fig. 7 (*a*) The values of λ, which correspond to $Q_{max}(x^*)$ shown in Fig. 6. These curves show which frequency corresponds to the most amplified disturbance at each value of x^*. (*b*) Neutral curves. The solid line with square symbols denotes the results for $c=2.5\times10^{-5}$ obtained by the finer grid, 960×96.

Table 1 Computed values of the neutral locations, (*A*) $c=10^{-4}$, (*B*) $c=5\times10^{-5}$, and (*C*) $c=2.5\times10^{-5}$, and comparison with Paul et al. [5]

	Neutral locations, x_c^*			
λ	*A*	*B*	*C*	Ref. [5]
0.5	355	500	506	543
0.55	469	630	638	673
0.6	590	773	773	797
0.65	724	903	896	919
0.7	851	1029	1021	1058
0.75	1191	1393	1377	1406

Table 1 shows the computed values of the neutral location against the disturbance frequency, λ, for the different values of c, where the corresponding values obtained by Paul et al. [5] are also shown. The results show that the neutral locations obtained using our sine-sweep simulations agree well with Ref. [5] especially for $c=5\times10^{-5}$ and $c=2.5\times10^{-5}$.

Figure 6 now displays the upper envelope of the curves shown in Figs. 4 and 5, where the envelope is defined as

$$Q_{\max}(x^*) = \max_{0.2\le\lambda\le0.45} Q(x^*,\lambda) \tag{19}$$

Thus $Q_{\max}(x^*)$ represents the maximum possible response of the boundary layer to thermal disturbances at each streamwise station. The values of the frequencies, which maximize Q and which are denoted by λ_{opt}, are shown in Fig. 7(*a*)—it is this figure that shows for which disturbance frequency, the largest disturbance amplitude, is obtained at a given downstream location.

The circles in Fig. 6 correspond to the previous computational results of Ref. [5] for disturbances of fixed frequency, while the dashed lines correspond to the results for $c=10^{-4}$, the dashed-dotted lines correspond to the results for $c=5\times10^{-5}$, and the solid lines correspond to the results for $c=2.5\times10^{-5}$. In addition, the solid line with square symbols in Figs. 6 and 7(*a*) corresponds to the results for $c=2.5\times10^{-5}$, which are obtained by the second grid setup, 960×96. It is clearly seen from these figures that the stability results obtained by both grid arrangements agree quite well and they are well resolved in the simulations.

The curves of $Q_{\max}$ obtained by the sine-sweep simulations lie slightly below the fixed frequency results [5]. The distance from the leading edge at which $Q_{\max}$ obtains its minimum values (Fig. 6) also varies with c (Table 2). This distance x^*, which disturbances are not amplified at all and which we refer to as "neutral distance" or "neutral point," decreases as c decreases; for ex-

Table 2 Distance from the leading edge at which $Q_{\max}$ obtains its minima (Fig. 6) and error relative to fixed frequency results

c	x^*	λ_{opt}	Error (%)
10^{-4}	126	0.262	4.4
5×10^{-5}	114	0.261	3.6
2.5×10^{-5}	109	0.255	1.2

ample, we have found that the neutral distance for $c=10^{-4}$ is $x^*=126$, while it is $x^*=114$ for $c=5\times10^{-5}$ and $x^*=109$ for $c=2.5\times10^{-5}$. The computations of Ref. [5] yield a value of the neutral distance of $x^*=105$, which clearly agrees quite well with the sine-sweep result for $c=2.5\times10^{-5}$. The corresponding values of the frequency at the neutral point obtained with the present method are about $\lambda=0.263$ for $c=10^{-4}$, $\lambda=0.261$ for $c=5\times10^{-5}$, and $\lambda=0.255$ for $c=2.5\times10^{-5}$, while the value obtained by Ref. [5] was about $\lambda=0.252$. So, the frequency result for $c=2.5\times10^{-5}$ also agrees quite well with the previous fixed frequency simulation.

The neutral curves for the different values of c are also presented in Fig. 7(*b*) against the disturbance frequency, and these are compared with those of the fixed frequency simulation [5], where again quite good agreement is found for $c=5\times10^{-5}$ and $c=2.5\times10^{-5}$ with Ref. [5].

The PFIs of Ref. [6] showed that the value of λ at the neutral point was about $\lambda=0.264$. Although the present result is closer to that of the PFI than to the constant frequency computation, our aim here is to see whether the sine-sweep computation can reproduce the constant frequency results sufficiently accurately using just one numerical simulation. Table 2 shows that the errors in the present computations are roughly 4.4% for $c=10^{-4}$, 3.6% for $c=5\times10^{-5}$, and 1.2% for $c=2.5\times10^{-5}$. Therefore, we conclude that the sine-sweep technique with a sufficiently small value of c (in this case, $c=2.5\times10^{-5}$) gives excellent results.

From the computational point of view, the total wall-clock time required to perform the sine-sweep code is much less than the constant frequency code. The total work done is proportional to the number of time steps taken in each code, as the amount of work done per time step is the same for the sine-sweep code and the fixed frequency code. It is likely that one requires simulations from more than 100 cases to achieve a well resolved neutral curve as shown in Ref. [6]. In the previous simulations of Ref. [5] with the selected discrete frequency we required about 10^5 time steps to achieve a periodic solution after the transient. We had to run the fixed frequency code 100 times to find the solutions for 100 frequencies. On the other hand, the present sine-sweep code with $c=2.5\times10^{-5}$ has saved about 86% of computational time compared with the fixed frequency code. The savings are even larger for the two larger values of c. We saved 92% of computational time with $c=5\times10^{-5}$ and 96% with $c=10^{-4}$. To conclude, the present sine-sweep code was found to not only accurately reproduce the fixed frequency code results but also results in significant computational time savings.

5 Conclusion

In this paper, we have reported on a numerical investigation in order to study the linear stability of a two-dimensional incompressible free convection boundary layer flow over a heated semi-infinite flat plate. A small-amplitude local temperature disturbance with slowly increasing frequency was introduced on the surface near the leading edge in order to generate disturbance waves inside the boundary layer. We have compared the stability characteristics obtained from the sine-sweep computations with those of the fixed frequency computations of Paul et al. [5] and with the PFI of Paul et al. [6].

As far as we are aware, this has been the first study where the sine-sweep technique has been used to assess the stability characteristics of a thermal boundary layer. It has been shown that this technique is an effective method for analyzing the stability of an advectively unstable boundary layer. Even larger savings can be expected from simulations with an entire frequency spectrum perturbed simultaneously as, e.g., by a pulse disturbance. This approach is possible as the problem studied here is linear and disturbance waves may be linearly superimposed.

Acknowledgment

The authors thank the anonymous referees for their valuable comments on the earlier version of this paper, which have served to improve the manuscript.

References

[1] Nachtsheim, P. R., 1963, "Stability of Free Convection Boundary Layer Flows," NASA Technical Report No. TN D-2089.

[2] Hieber, C. A., and Gebhart, B., 1971, "Stability of Vertical Natural Convection Boundary Layers," J. Fluid Mech., **48**, pp. 625–646.

[3] Goldstein, M. E., 1983, "The Evolution of Tollmien-Schlichting Waves Near a Leading Edge," J. Fluid Mech., **127**, pp. 59–81.

[4] Paul, M. C., 2002, "The Stability of Free Convective Boundary Layer Flows," Ph.D. thesis, University of Bath, UK.

[5] Paul, M. C., Rees, D. A. S., and Wilson, M., 2007, "Thermal Receptivity of Free Convective Flow From a Heated Vertical Surface: Linear Waves," Int. J. Therm. Sci., **47**, pp. 1382–1392.

[6] Paul, M. C., Rees, D. A. S., and Wilson, M., 2005, "The Influence of Higher Order Effects on the Linear Wave Instability of Vertical Free Convective Boundary Layer Flow," Int. J. Heat Mass Transfer, **48**, pp. 809–817.

[7] Fasel, H., and Konzelmann, U., 1990, "Non-Parallel Stability of a Flat-Plate Boundary Layer Using the Complete Navier-Stokes Equations," J. Fluid Mech., **221**, pp. 311–347.

[8] Brooker, A. M. H., Patterson, J. C., and Armfield, S. W., 1997, "Non-Parallel Linear Stability Analysis of the Vertical Boundary Layer in a Differentially Heated Cavity," J. Fluid Mech., **352**, pp. 265–281.

[9] Dietz, A. J., 1999, "Local Boundary-Layer Receptivity to a Convected Free-Stream Disturbance," J. Fluid Mech., **378**, pp. 291–317.

[10] Arakawa, A., 1966, "Computational Design of Long-Term Numerical Integration of the Equations of Fluid Motion: I. Two Dimensional Incompressible Flow," J. Comput. Phys., **1**, pp. 119–143.

[11] Briggs, W., 1987, *A Multigrid Tutorial*, S.I.A.M., Philadelphia.

[12] Kloker, M., Konzelmann, U., and Fasel, H., 1993, "Outflow Boundary Conditions for Spatial Navier-Stokes Simulations of Transitional Boundary Layers," AIAA J., **31**, pp. 620–628.

[13] Stemmer, C., Kloker, M., and Wagner, S., 2000, "Navier-Stokes Simulation of Harmonic Point Disturbances in an Airfoil Boundary Layer," AIAA J., **38**, pp. 1369–1376.

[14] Bake, S., Meyer, G., and Rist, U., 2002, "Turbulence Mechanism in Klebanoff Transition: A Quantitative Comparison of Experiment and Direct Numerical Simulation," J. Fluid Mech., **459**, pp. 217–243.